arXiv:1905.06854v1 [physics.comp-ph] 15 May 2019

Neutron Transmission Strain Tomography for Non-Constant Strain-Free Lattice Spacing

J.N. Hendriks[1], C. Jidling[2], T.B. Schön[2], A. Wills[1], C.M. Wensrich[1], and E.H. Kisi[1]

[1]*School of Engineering, The University of Newcastle, Callaghan NSW 2308, Australia*
[2]*Department of Information Technology, Uppsala University, Sweden*

April 15, 2022

Abstract

Recently, several algorithms for strain tomography from energy-resolved neutron transmission measurements have been proposed. These methods assume that the strain-free lattice spacing d_0 is a known constant limiting their application to the study of stresses generated by manufacturing and loading methods that do not alter this parameter. In this paper, we consider the more general problem of jointly reconstructing the strain and d_0 fields. A method for solving this inherently non-linear problem is presented that ensures the estimated strain field satisfies equilibrium and can include knowledge of boundary conditions. This method is tested on a simulated data set with realistic noise levels, demonstrating that it is possible to jointly reconstruct d_0 and the strain field.

1 Introduction

Energy-resolved neutron transmission methods can generate lower dimensional (one- or two-dimensional) images of strain from a higher dimensional (two- or three-dimensional) strain field within a polycrystalline material. The 'tomographic' reconstruction of an unknown strain field from these images can be used to study the residual strain and stress within engineering components. Residual stresses are those which remain after applied loads are removed (e.g. due to heat treatment, plastic deformation, etc.), and may have significant and unintended impact on a component's effective strength and service life — in particular its fatigue life. Measuring and quantifying these strains is important for the validation of predictive design tools, such as Finite Element Analysis, and to aid the development of novel manufacturing techniques — i.e. additive manufacturing.

These strain images are generated by analysing features known as Bragg-edges in the relative transmission of a neutron pulse through a sample. Bragg-edges are sudden increases in the intensity as a function of wavelength and occur when the scattering angle 2ϑ reaches 180°, beyond which no further coherent scattering can occur. The wavelength λ at which these Bragg-edges occur can be related to the lattice spacing d within the sample through Bragg's law: $\lambda = 2d\sin\vartheta$. Assuming minimal texture, this can be used to provide a relative measure of strain;

$$\langle\epsilon\rangle = \frac{d - d_0}{d_0}, \tag{1}$$

where d_0 is the strain-free lattice spacing and $\langle\epsilon\rangle$ is a through thickness average of the normal, elastic strain in the direction of the beam.

The determination of d_0 is a problem inherent to diffraction and transmission strain analysis. For specific cases where the loading mechanism does not result in changes to the strain-free lattice parameter, its value can be measured prior to loading and in the simplest case (e.g. for an annealed sample) a constant value throughout the sample can be assumed. Several algorithms for strain tomography assuming a known, constant strain-free lattice spacing have been developed. Reconstruction of axisymmetric strain fields is considered in

(Abbey et al., 2009, 2012; Kirkwood et al., 2015; Gregg et al., 2017) and more general two-dimensional strain fields in (Gregg et al., 2018; Jidling et al., 2018; Hendriks et al., 2018a).

Many manufacturing techniques (e.g. welding and additive manufacturing) can alter the lattice spacing; for example, as a result of inhomogeneously distributed phase changes (such as the Martensite transformation), or due to gradients in composition as a result of differing chemical states in the starting materials. Since the lattice spacing (in this case d_0) is sensitive to crystal structure and composition changes, the strain-free lattice parameter may vary throughout the sample. Ignoring variations in d_0 would cause severe degradation in the quality of a reconstructed strain field. In such cases, measuring d_0 is more challenging and has been achieved in neutron diffraction measurements by measuring additional directions of strain (Luzin et al., 2011; Choi et al., 2007) and by destructive methods where the strain is relieved by wire cutting the sample into a grid allowing the strain-free lattice spacing to be measured throughout the sample (Paradowska et al., 2005). Although the latter of these two options could be applied to strain tomography it requires the destruction of the sample and creates an additional tomography problem, requiring another set of measurements to be acquired.

Here, we present a method capable of jointly reconstructing the strain field and the d_0 field from a single set of neutron transmission images. To achieve this both the strain and d_0 are modelled by a Gaussian process (see for example Rasmussen and Williams (2006)) and equilibrium and boundary conditions are built into the strain model (Jidling et al., 2017). This extends the Gaussian process approach presented by Jidling et al. (2018); Hendriks et al. (2018a) to handle the inherently non-linear nature of this problem. A numerically tractable algorithm based on variational inference (see for example Blei et al. (2017); Jordan et al. (1999)) is provided and the method is validated on a simulated data set.

2 Problem Statement

This paper focuses on the joint reconstruction of the strain field $\boldsymbol{\epsilon}(\mathbf{x})$ and a non-constant strain-free lattice parameter $d_0(\mathbf{x})$ from a set of neutron transmission images. Restricting the problem to two dimensions, gives the strain field as the symmetric tensor

$$\boldsymbol{\epsilon}(\mathbf{x}) = \begin{bmatrix} \epsilon_{xx}(\mathbf{x}) & \epsilon_{xy}(\mathbf{x}) \\ \epsilon_{xy}(\mathbf{x}) & \epsilon_{yy}(\mathbf{x}) \end{bmatrix}, \tag{2}$$

where $\mathbf{x} = \begin{bmatrix} x & y \end{bmatrix}^\mathsf{T}$. For brevity, the unique components of strain will be written as $\bar{\epsilon} = \begin{bmatrix} \epsilon_{xx} & \epsilon_{xy} & \epsilon_{yy} \end{bmatrix}^\mathsf{T}$ with the coordinate $\mathbf{x}$ omitted where appropriate.

Here, we consider the lattice spacings d as the measurements rather than the standard approach which considers the relative strain of the form form (1). This allows the measurements to be explicitly related to both the strain and the strain-free lattice parameter through the Longitudinal Ray Transform (LRT) (Lionheart and Withers, 2015):

$$y(\boldsymbol{\eta}) = d(\boldsymbol{\eta}) + e = \frac{1}{L} \int_0^L \bar{\mathbf{n}} \bar{\boldsymbol{\epsilon}}(\mathbf{p} + \hat{\mathbf{n}}s) d_0(\mathbf{p} + \hat{\mathbf{n}}s) + d_0(\mathbf{p} + \hat{\mathbf{n}}s) \, \mathrm{d}s + e. \tag{3}$$

where $e \sim \mathcal{N}(0, \sigma_n^2)$ and the geometry of each measurement is given by the parameter set $\boldsymbol{\eta} = \{\hat{\mathbf{n}}, L, \mathbf{p}\}$; with $\hat{\mathbf{n}}$ as the beam direction, L as the irradiation length, $\mathbf{p} = \begin{bmatrix} x_0 & y_0 \end{bmatrix}^\mathsf{T}$ as the point of initial intersection between the ray and the sample, and $\bar{\mathbf{n}} = \begin{bmatrix} \hat{n}_1^2 & 2\hat{n}_1\hat{n}_2 & \hat{n}_2^2 \end{bmatrix}$. See Figure 1 for the measurement geometry. These measurements are a non-linear function of the two phenomena we wish to estimate; $\boldsymbol{\epsilon}$ and d_0.

For details on the analysis of neutron transmission data to determine these lattice spacings the reader is referred to Santisteban et al. (2002b,a); Tremsin et al. (2011, 2012). It is also worth noting that the standard deviation σ_n of these measurements is available.

Furthermore, the strain field inside a sample is a physical property and as such it is subject to equilibrium and boundary conditions (Sadd, 2009). Therefore, it is natural to constrain estimates of the strain field to

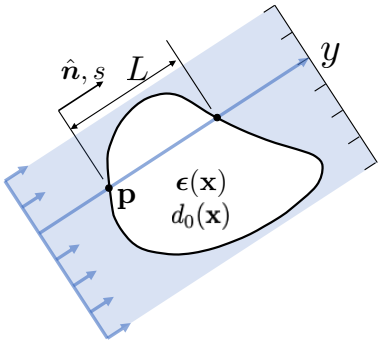


Figure 1: LRT measurement geometry. Each measurement made by a detector pixel is associated with a ray of direction $\hat{\mathbf{n}}$ that enters the sample at $\mathbf{p}$ and has a total irradiated length of L.

satisfy these conditions. Using Hooke's law the equilibrium conditions can be written directly in terms of strain. In two dimensions, this relies on an assumption of plane strain or plane stress. Plane stress is assumed for the remainder of this work, giving the equilibrium conditions as

$$\begin{aligned} \frac{\partial}{\partial x}(\epsilon_{xx} + \nu\epsilon_{yy}) + \frac{\partial}{\partial y}(1-\nu)\epsilon_{xy} = 0, \\ \frac{\partial}{\partial x}(\epsilon_{yy} + \nu\epsilon_{xx}) + \frac{\partial}{\partial y}(1-\nu)\epsilon_{xy} = 0, \end{aligned} \tag{4}$$

where ν is Poisson's ratio.

Boundary conditions, in particular the load free surfaces, may also be known. For an unloaded surface, the distribution of forces known as tractions will be zero. Through equilibrium this places additional linear constraints on the strain field, which, assuming plane stress, can be written as

$$\mathbf{0} = \begin{bmatrix} n_{\perp 1} & n_{\perp 2} & 0 \\ 0 & n_{\perp 1} & n_{\perp 2} \end{bmatrix} \begin{bmatrix} 1 & 0 & -\nu \\ 0 & 1+\nu & 0 \\ -\nu & 0 & 1 \end{bmatrix} \bar{\boldsymbol{\epsilon}}(\mathbf{x}_b), \tag{5}$$

where $\mathbf{x}_b$ is a point on an unloaded surface and $\mathbf{n}_\perp$ is the normal to the surface at this point.

An approach to enforcing equilibrium in the estimated strain field is to define a Gaussian process for the Airys stress function from which strain can be derived (Jidling et al., 2018). This non-parametric approach was demonstrated experimentally by Jidling et al. (2018) and compared to other parametric approaches by Hendriks et al. (2018a) with promising results. Boundary conditions in the form of (5) can be included in the estimation process as artificial measurements of zero traction (Hendriks et al., 2018a).

We wish to extend this approach so that both the strain field and the strain-free lattice spacing can be estimated. As the measurements are a non-linear function of the unknowns we cannot directly apply the standard Gaussian process regression methods (Rasmussen and Williams, 2006). There exists several approaches to approximate Gaussian processes for non-linear functions; the Laplace approximation (Rasmussen and Williams, 2006; Bishop et al., 1995), GP variational inference (Steinberg and Bonilla, 2014), and Markov Chain Monte Carlo methods (such as Elliptical Slice Sampling (Murray and Adams, 2010)). For these methods, the measurements are modelled as non-linear functions of the GP sampled at the measurement locations (known as latent function values). The latent function values that best[1] match the data are determined by one of the above methods. Then, Gaussian process regression is applied with the latent function values taking the place of measurements to determine the function values at the new locations of interest.

The non-static nature of the integral measurement model (3) makes it unclear how to express the measurements as a function of a finite set of latent function values, and hence the above approaches to approximating the GP for non-linear measurements cannot be applied directly. In the following section, we utilise an finite

[1]For a given criterion of best fit, whether it be marginal log likelihood, cross-validation, etc.

basis function approximation to the GP, and by viewing the problem from an alternate perspective we show how variational inference can be used to solve this non-linear problem.

3 Method

The method presented here is to define a Gaussian process model for the strain field and the strain-free lattice spacing. This Gaussian process model is then approximated using a Hilbert space approximation (Solin and Särkkä, 2014; Jidling et al., 2018). This has two benefits; firstly it removes the need for numerical integration of the covariance function (as discussed by Jidling et al. (2018, 2017)), and secondly it allows us to reformulate the problem as a set of basis functions with unknown coefficients. Variational inference can then be used to learn the coefficients from the LRT measurements and artificial measurements of zero traction.

3.1 Gaussian Process model

The Gaussian process (GP) is a Gaussian distribution of spatially correlated functions;

$$f(\mathbf{x}) \sim \mathcal{GP}\left(m(\mathbf{x}), k(\mathbf{x}, \mathbf{x}')\right). \tag{6}$$

The characteristics of the functions belonging to this distribution are governed by a mean function $m(\mathbf{x})$ and a covariance function $k(\mathbf{x}, \mathbf{x}')$. The covariance function describes the correlation between the function values $f(\mathbf{x})$ and $f(\mathbf{x}')$ at any two points $\mathbf{x}$ and $\mathbf{x}'$. Careful design of the covariance function can ensure that only functions satisfying desired characteristics belong to the distribution.

Here, we wish to design the covariance function to ensure that only strain fields satisfying equilibrium are contained in the GP prior. Following the formulation in (Jidling et al., 2018) a GP model for the Airys stress functions is defined; $\varphi(\mathbf{x}) \sim \mathcal{GP}\left(0, k_\varphi(\mathbf{x}, \mathbf{x}')\right)$. Under the assumption that the sample is plane stress, isotropic, and contiguous, the Airy's stress functions can be related to strain through the mapping

$$\bar{\boldsymbol{\epsilon}}(\mathbf{x}) = \mathcal{V}^{\mathbf{x}}\varphi(\mathbf{x}), \qquad \mathcal{V}^{\mathbf{x}} = \begin{bmatrix} \frac{\partial^2}{\partial y^2} - \nu\frac{\partial^2}{\partial x^2} \\ -(1+\nu)\frac{\partial^2}{\partial x \partial y} \\ \frac{\partial^2}{\partial x^2} - \nu\frac{\partial^2}{\partial y^2} \end{bmatrix}, \tag{7}$$

where $\mathcal{V}$ is a linear operator, and the superscript denotes which variable the operator acts on. As GPs are closed under linear operators (Papoulis and Pillai, 2002; Hennig and Kiefel, 2013; Wahlström, 2015; Jidling et al., 2018) a GP model for strain that satisfies equilibrium can now be defined;

$$\bar{\boldsymbol{\epsilon}}(\mathbf{x}) \sim \mathcal{GP}\left(0, \mathcal{V}^{\mathbf{x}} k_\varphi(\mathbf{x}, \mathbf{x}') \mathcal{V}^{\mathbf{x}'\mathsf{T}}\right), \tag{8}$$

where a prior mean function of zero has been chosen.

Additionally, d_0 function is also modelled by a GP;

$$d_0(\mathbf{x}) \sim \mathcal{GP}(\bar{d}_0, k_{d_0}(\mathbf{x}, \mathbf{x}')). \tag{9}$$

where the prior mean $\bar{d}_0$ is chosen to be close to the expected theoretical strain-free lattice spacing for the material used or a measured average in a strain-free sample. The choice of prior mean function does not mean that we believe the d_0 and $\bar{\boldsymbol{\epsilon}}$ functions to be a particular value, but rather that we do not have any information to suggest otherwise. After the inclusion of measurement information, the mean of the posterior estimate will be updated.

There exists a number of options for the base covariance functions $k_\varphi(\mathbf{x}, \mathbf{x}')$ and $k_{d_0}(\mathbf{x}, \mathbf{x}')$, with both the squared-exponential and the Matérn covariance functions having been successfully used for strain estimation

(Jidling et al., 2018; Hendriks et al., 2018a). For a more thorough discourse on available covariance functions the reader is referred to Rasmussen and Williams (2006).

Having defined suitable GP models for the strain and d_0 fields we now wish to estimate these fields from the LRT and traction measurements. However, the LRT is a non-linear function of these fields and consequently a closed form solution does not exist. The following presents a method for obtaining these estimates that approximates the GP by a finite number of basis functions allowing variational inference to be applied.

3.2 Hilbert Space Approximation to the GP Prior

Here, we make use of the approximation method proposed by (Solin and Särkkä, 2014) and demonstrated to be suitable for the problem of strain tomography (Jidling et al., 2018). This method approximates our covariance function by a finite sum of m basis functions;

$$k(\mathbf{x}, \mathbf{x}') = \sum_{j=1}^{m} \phi_i(\mathbf{x}) S(\boldsymbol{\lambda}_j) \phi_j(\mathbf{x}'), \tag{10}$$

where S is the spectral density of the covariance function. For a stationary covariance function $k = k(\mathbf{r})$, where $\mathbf{r} = \mathbf{x} - \mathbf{x}'$, the spectral density and the basis functions are given by;

$$S(\boldsymbol{\omega}) = \int k(\mathbf{r}) e^{-i\boldsymbol{\omega}^\mathsf{T}\mathbf{r}} \,\mathrm{d}\mathbf{r}, \quad \phi_j = \frac{1}{\sqrt{L_x L_y}} \sin(\lambda_{x,j}(x + L_x)) \sin(\lambda_{y,j}(y + L_y)), \tag{11}$$

where L_x and L_y control the domain size, and $\boldsymbol{\lambda} = [\lambda_x, \lambda_y]^\mathsf{T}$ encodes spatial frequencies of the basis functions. The basis functions are chosen as a solution to the Dirichlet boundary conditions on a rectangular domain, which is a natural choice for the Laplace eigenvalue problem that needs to be solved to approximate the GP (Jidling et al., 2018). The parameters $\theta = \{l_x, l_y, \sigma_f\}$ are commonly called 'hyperparameters' and can be chosen by optimisation (as discussed in Section 5.2). For our application the domain size and spatial frequencies are chosen such that the basis functions spanned a region where their spectral densities, were greater than a minimum threshold. This helps to ensure that the dominant frequencies of the response are captured while maintaining numerical stability.

At this stage, the alternative view point of Bayesian linear regression can be taken. This approach models the unknown function by a set of basis functions with Gaussian coefficients;

$$f(\mathbf{x}) = \sum_{j=1}^{m} \phi_j(\mathbf{x}) w_j = \boldsymbol{\phi}(\mathbf{x})\mathbf{w}, \qquad w_j \sim \mathcal{N}(\mu_j, S(\boldsymbol{\lambda}_j)), \tag{12}$$

where $\boldsymbol{\phi}(\mathbf{x})$ and $\mathbf{w}$ have dimensions $[1, m]$ and $[m, 1]$, respectively. This gives the following model for the strain field $\bar{\boldsymbol{\epsilon}}(\mathbf{x})$ and the strain-free lattice spacing $d_0(\mathbf{x})$;

$$\begin{aligned}
&\bar{\boldsymbol{\epsilon}}_*(\mathbf{x}) = \boldsymbol{\phi}_\epsilon \mathbf{w}_\varphi, \quad \phi_{\epsilon,j}(\mathbf{x}) = \mathcal{V}^{\mathbf{x}} \phi_{\varphi,j}(\mathbf{x}), \quad \phi_{\varphi,j} = \frac{1}{\sqrt{L_{\varphi x} L_{\varphi y}}} \sin(\lambda_{\varphi x,j}(x + L_{\varphi x})) \sin(\lambda_{\varphi y,j}(y + L_{\varphi y})), \\
&d_{0*}(\mathbf{x}) = \boldsymbol{\phi}_{d_0} \mathbf{w}_{d_0}, \quad \phi_{d_0,k}(\mathbf{x}) = \frac{1}{\sqrt{L_{d_0 x} L_{d_0 y}}} \sin(\lambda_{d_0 x,k}(x + L_{d_0 x})) \sin(\lambda_{d_0 y,k}(y + L_{d_0 y})),
\end{aligned} \tag{13}$$

where the unknown coefficients are independently normally distributed to approximate our GP model; $w_{\varphi,j} \sim \mathcal{N}(0, S_\varphi(\boldsymbol{\lambda}_{\varphi,j}))$ and $w_{d_0,j} \sim \mathcal{N}(\mu_{d_0,j}, S_{d_0}(\boldsymbol{\lambda}_{d_0,j}))$. Where the means $\mu_{d_0,j}$ are chosen so that the prior has the constant value $\bar{d}_0$. In this work, basis functions and parameters corresponding to the d_0 field will be denoted by the subscript d_0 and the subscript k will be used as an index. Likewise, basis functions and parameters corresponding to the Airys stress function will be denoted by the subscript d_0 and the subscript j will be used as an index. The expanded expressions for $\boldsymbol{\phi}_\epsilon$ are given in Appendix A.

Using the LRT (3) we can write a model for a predicted measurement as a non-linear function of the unknown coefficients;

$$\begin{aligned} y_* &= \frac{1}{L}\int_0^L \bar{\mathbf{n}}\left(\sum_j\sum_k \phi_{\epsilon,j}(\mathbf{p}+\hat{\mathbf{n}}s)w_{\varphi,j}\phi_{d_0,k}(\mathbf{p}+\hat{n}s)w_{d_0,k}\right)+\left(\sum_k \phi_{d_0,k}(\mathbf{p}+\hat{n}s)w_{d_0,k}\right)\mathrm{d}s \\ &= g_y(\mathbf{w}_\varphi, \mathbf{w}_{d_0}, \boldsymbol{\eta}), \end{aligned} \tag{14}$$

where we have restricted ourselves to a single measurement to simplify the notation. These integrals can be analytically evaluated and the equations are given in Appendix A. Predictions of the boundary tractions $\mathbf{y}_t$ at a boundary location $\mathbf{x}_b$ with surface normal $\mathbf{n}_\perp$ can be written as a linear function of the unknown coefficients;

$$\begin{aligned} y_{t*} &= \underbrace{\begin{bmatrix} n_{\perp 1} & n_{\perp 2} & 0 \\ 0 & n_{\perp 1} & n_{\perp 2} \end{bmatrix}}_{\mathbf{T}} \boldsymbol{\phi}_\varphi(\mathbf{x})\mathbf{w}_\varphi = \mathbf{T}(\mathbf{n}_\perp)\boldsymbol{\phi}_\varphi(\mathbf{x}_b)\mathbf{w}_\varphi \\ &= g_t(\mathbf{w}, \mathbf{x}_b, \mathbf{n}_\perp). \end{aligned} \tag{15}$$

The coefficients $\mathbf{w}_\varphi$ and $\mathbf{w}_{d_0}$ are random variables; as such the predictions $\bar{\boldsymbol{\epsilon}}_*$, y_*, and y_{t*} are also random variables. The problem now is to determine the distribution of the coefficients given a set of LRT and traction measurements. This problem is now in a form allowing variational inference to be used to approximate a solution to the non-linear problem.

3.3 Variational Inference

Variational inference (Blei et al., 2017; Jordan et al., 1999) provides an approximation to the posterior distribution by assuming that it has a certain functional form that contain unknown parameters. These unknown parameters are found using optimization, where some distance measure is minimized. We will in this section provide the details enabling the use of variational inference in solving our problem.

Given n transmission measurements and n_t traction measurements, such that a vector of all measurements is given by $\mathbf{Y} = [y_1, \ldots, y_n, y_{t,1}, \ldots, y_{t,n_t}]^\mathsf{T}$, the problem can be written as having prior and likelihood

$$p(\mathbf{w}) \sim \mathcal{N}(\boldsymbol{\mu}, \boldsymbol{\Sigma}_p) \quad \text{and} \quad p(\mathbf{Y}|\mathbf{w}) \sim \mathcal{N}(\mathbf{Y}|g(\mathbf{w}), \boldsymbol{\Sigma}_n), \tag{16}$$

where $\mathbf{w} = \begin{bmatrix}\mathbf{w}_{d_0}^\mathsf{T} & \mathbf{w}_\varphi^\mathsf{T}\end{bmatrix}^\mathsf{T}$, $\boldsymbol{\mu}$ is a vector of all the prior means, and $\boldsymbol{\Sigma}_p$ is a matrix with the coefficients prior variance on the diagonals. Here, $g(\cdot)$ is the combined measurement model that expresses the measurement vector $\mathbf{Y}$ as a function of the coefficients. This function is constructed using both (14) and (15). Finally, $\boldsymbol{\Sigma}_n = \mathrm{diag}(\sigma_n^2 I_{n\times n}, \sigma_t^2 I_{n_t\times n_t})$, where σ_t^2 is a small variance placed on the artificial traction measurements added for numerical reasons.

The non-linear measurement function $g(\cdot)$ makes the likelihood intractable as the prior and likelihood are no longer conjugate. Consequently, the posterior $p(\mathbf{w}|\mathbf{Y})$ is also intractable and so we find an approximate solution using variational inference (Jordan et al., 1999). The idea is to approximate the true posterior by the Gaussian distribution $q(\mathbf{w}) \sim \mathcal{N}(\hat{\mathbf{w}}, \mathbf{C})$, and find the mean $\hat{\mathbf{w}}$ and covariance $\mathbf{C}$ for this distribution that maximise the Free Energy $\mathcal{F}$. The Free Energy places a lower bound on the log marginal likelihood and hence provides a measure of how well our posterior fits the data;

$$\log p(\mathbf{Y}) \geq \mathbb{E}\left[\log p(\mathbf{Y}|\mathbf{W})\right] - KL\left[q(\mathbf{w})||p(\mathbf{w}|\mathbf{Y})\right] = \mathcal{F} \tag{17}$$

where, in this case, $\mathbb{E}[\cdot]$ is the expected value with respect to the approximate posterior $q(\mathbf{w})$ and $KL[\cdot]$ is the Kullback Leibler divergence which provides a measure of difference between the approximate posterior and the true posterior. These terms can be evaluated as (Steinberg and Bonilla, 2014);

$$\begin{aligned} \mathbb{E}\left[\log p(\mathbf{Y}|\mathbf{W})\right] &= \frac{1}{2}\left[N\log 2\pi + \log|\boldsymbol{\Sigma}_n| + (\mathbf{Y}-\mathbb{E}\left[g(\mathbf{w})\right])^\mathsf{T}\boldsymbol{\Sigma}_n^{-1}(\mathbf{Y}-\mathbb{E}\left[g(\mathbf{w})\right])\right], \\ KL\left[q(\mathbf{w})||p(\mathbf{w}|\mathbf{Y})\right] &= \frac{1}{2}\left[\mathrm{tr}(\boldsymbol{\Sigma}_p^{-1}\mathbf{C}) + (\boldsymbol{\mu}-\hat{\mathbf{w}})^\mathsf{T}\boldsymbol{\Sigma}_p^{-1}(\boldsymbol{\mu}-\hat{\mathbf{w}}) - \log|\mathbf{C}| + \log|\boldsymbol{\Sigma}_p| - N\right], \end{aligned} \tag{18}$$

where $N = n + n_t$. Here, the expectation of the non-linear function $\mathbb{E}[g(\mathbf{w})]$ is intractable (Steinberg and Bonilla, 2014) and so the expected maximum is used $\hat{\mathbf{Y}} = g(\hat{\mathbf{w}})$;

$$\mathcal{F} \approx -\frac{1}{2}\left[N \log 2\pi + \log|\boldsymbol{\Sigma}_n| - \log|\mathbf{C}| + \log|\boldsymbol{\Sigma}_p| + (\mathbf{Y} - g(\hat{\mathbf{w}}))^\mathsf{T} \boldsymbol{\Sigma}_n^{-1} (\mathbf{Y} - g(\hat{\mathbf{w}})) + (\boldsymbol{\mu} - \hat{\mathbf{w}})^\mathsf{T} \boldsymbol{\Sigma}_p^{-1} (\boldsymbol{\mu} - \hat{\mathbf{w}})\right] \tag{19}$$

The optimal posterior mean is chosen to maximise the Free Energy. To perform this optimisation a modified Newton's method is used where the step direction is $\mathbf{q} = -\mathbf{H}^{-1}\mathbf{g}$ and we can calculate the gradient, $\mathbf{g}$, and Hessian, $\mathbf{H}$, of the cost as

$$\begin{aligned} \mathbf{g} &= \mathbf{J}^\mathsf{T} \boldsymbol{\Sigma}_n^{-1} (\mathbf{Y} - g(\hat{\mathbf{w}})) - \boldsymbol{\Sigma}_p^{-1} \hat{\mathbf{w}} \\ \mathbf{H} &= -\mathbf{J}^\mathsf{T} \boldsymbol{\Sigma}_n^{-1} \mathbf{J} + \frac{\partial \mathbf{J}^\mathsf{T}}{\partial \mathbf{w}} \Sigma_n^{-1} (\mathbf{Y} - g(\hat{\mathbf{w}})) - \boldsymbol{\Sigma}_p^{-1} \end{aligned} \tag{20}$$

where $\mathbf{J} = \begin{bmatrix} \frac{\partial \hat{\mathbf{Y}}}{\partial \hat{\mathbf{w}}}^\mathsf{T} & \frac{\partial \hat{\mathbf{Y}}_t}{\partial \hat{\mathbf{w}}}^\mathsf{T} \end{bmatrix}^\mathsf{T}$, and the derivatives and second derivatives are given in Appendix B. At each iteration we update the coefficients according to

$$\hat{\mathbf{w}}_{k+1} = (1 - \alpha)\hat{\mathbf{w}}_k + \alpha \mathbf{q} + \alpha \boldsymbol{\mu}, \tag{21}$$

A backwards line search is used to ensure that $\mathcal{F}$ is increased in each iteration. Once the optimal posterior mean is found, the covariance can be found by setting $\frac{\partial \mathcal{F}}{\partial \mathbf{C}} = 0$ and linearising about $\hat{\mathbf{w}}$ (Steinberg and Bonilla, 2014), giving;

$$\mathbf{C} = \left[\boldsymbol{\Sigma}_p^{-1} + \mathbf{J}^\mathsf{T} \Sigma_n^{-1} \mathbf{J}\right]^{-1}. \tag{22}$$

Pseudo-code for an algorithm to find approximate distribution of the coefficients $q(\mathbf{w}) \sim \mathcal{N}(\hat{\mathbf{w}}, \mathbf{C})$ is given in Algorithm 1. Once the coefficients are found, estimates of the strain and d_0 fields can be estimated. The approximate poster mean and variance for the strain field and strain-free lattice spacing can be computed as

$$\begin{aligned} \begin{bmatrix} \hat{d}_0(\mathbf{x}) \\ \hat{\tilde{\boldsymbol{\epsilon}}} \end{bmatrix} &= \begin{bmatrix} \boldsymbol{\phi}_\epsilon(\mathbf{x}) & 0 \\ 0 & \boldsymbol{\phi}_\epsilon(\mathbf{x}) \end{bmatrix} \hat{\mathbf{w}}, \\ \hat{\Sigma} &= \begin{bmatrix} \boldsymbol{\phi}_\epsilon(\mathbf{x}) & 0 \\ 0 & \boldsymbol{\phi}_\epsilon(\mathbf{x}) \end{bmatrix} \mathbf{C} \begin{bmatrix} \boldsymbol{\phi}_\epsilon(\mathbf{x}) & 0 \\ 0 & \boldsymbol{\phi}_\epsilon(\mathbf{x}) \end{bmatrix}^\mathsf{T}, \end{aligned} \tag{23}$$

where $\hat{\Sigma}$ is the joint covariance of the strain and d_0 estimates. Next, this method is demonstrated on a set of measurements simulated from a theoretical cantilever beam strain field and an artificial d_0 field.

Algorithm 1 Variational inference algorithm for finding the coefficients $q(\mathbf{w}) \sim \mathcal{N}(\hat{\mathbf{w}}, \mathbf{C})$. Requires the hyperparameters θ, the specified number of basis functions m_φ and m_{d_0}, the LRT measurement information $\{y_i, \boldsymbol{\eta}_i | \forall i = 1, \ldots, n\}$ and the boundary traction information $\{y_{t,i} = 0, \mathbf{x}_{b,i}, \mathbf{n}_{\perp,i} | \forall i = 1, \ldots, n_t\}$.

procedure FIND COEFFICIENTS
  Compute the basis functions for the LRT measurements using Equation 14
  Compute the basis functions for the traction measurements using Equation 15
  Build prior variance $\boldsymbol{\Sigma}_p$
  Initialise the coefficients $\hat{\mathbf{w}}_1$
  set $k = 1$
  while Stopping criteria not met **do**
    Compute the gradient $\mathbf{g}$ and Hessian $\mathbf{H}$ linearised about $\hat{\mathbf{w}}_k$ according to Equation 20
    Calculate $\hat{\mathbf{w}}_{k+1}$ using Equation 21 and a backward line search
    $k = k + 1$
  end while
  Calculate the covariance $\mathbf{C}$ according to Equation 22
  return $\hat{\mathbf{w}}_k$ and $\mathbf{C}$
end procedure

4 Simulation Results

The method's ability to jointly reconstruct the strain field and a d_0 field is demonstrated using simulated measurements. Reconstructions from measurements simulated through two strain fields is shown; the Saint-Venant approximate strain field for a cantilver beam, and a Finite Element Analysis (FEA) strain field from an in-situ loaded C-shape. Additionally, the consequences of ignoring the d_0 variation on the reconstruction are shown by using the linear measurement model and Gaussian process regression method presented by Jidling et al. (2018) with the addition of traction constraints as shown in Hendriks et al. (2018a). Matlab code to run both examples can be found on Github (Hendriks, 2019).

4.1 Cantilever Beam Example

The method is first demonstrated for the theoretical Saint-Venant cantilever beam as studied. Assuming plane stress, the Saint-Venant approximation to the strain field is (Beer et al., 2010):

$$\boldsymbol{\mathcal{E}}(\mathbf{x}) = \begin{bmatrix} \frac{P}{EI}(L-x)y \\ -\frac{(1+\nu)P}{2EI}\left(\left(\frac{h}{2}\right)^2 - y^2\right) \\ -\frac{\nu P}{EI}(L-x)y \end{bmatrix}, \tag{24}$$

where the geometry is defined in Figure 2. A synthetic strain-free lattice spacing field is defined by

$$d_0(\mathbf{x}) = c_0 \exp\left(-\frac{1}{2}(x-c_1)^2/c_2^2 - \frac{1}{2}(y-c_3)^2/c_4^2\right) + c_5, \tag{25}$$

with the parameters given by $\{c_0, c_1, c_2, c_3, c_4, c_5\} = \{0.0168, 0, 7.5\times10^{-3}, 7\times10^{-3}, 6\times10^{-3}, 4.056\}$. The maximum variation c_0 from a constant base value, c_5, was chosen to reflect the possible maximum relative variation due to martensitic phase change in 0.8% carbon steel.

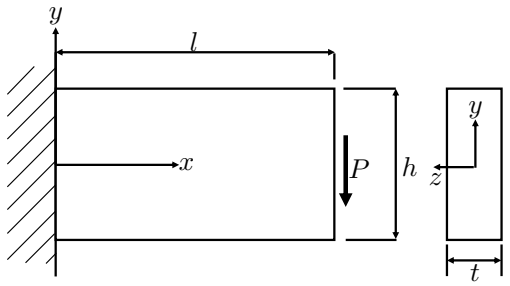


Figure 2: Cantilever beam geometry and coordinate system with $l = 20$mm, $h = 10$mm, $t = 5$mm, $E = 200$GPa, $P = 2$kN, $\nu = 0.28$, and $I = \frac{th^3}{12}$.

Measurements of the form (3) were simulated for 30 angles evenly spaced between 0° and 180°, with 100 measurements per angle, which is on the conservative side based on past experiments (Gregg et al., 2018; Hendriks et al., 2017). The simulated measurements were corrupted with zero-mean noise of standard deviation $\sigma_n = c_5 \times 10^{-4}$ which is equilvalent to 1×10^{-4} standard deviation in strain representing the typical experimental noise (Hendriks et al., 2017; Gregg et al., 2018)

Fifty zero-traction measurements were added along the top and bottom of the cantilever beam for both the presented method and the linear GP regression method. Results are shown in Figure 3. These results show that the presented method successfully reconstructs both the strain field and the d_0 field with a relative error[2] of 0.0057. By contrast ignoring the presence of a d_0 variation and using a linear GP regression method yields a drastically degraded strain reconstruction with a relative error of 0.3067.

[2] relative error $= \frac{\text{mean}(|\text{true}-\text{estimated}|)}{\max(|\text{true}|)}$

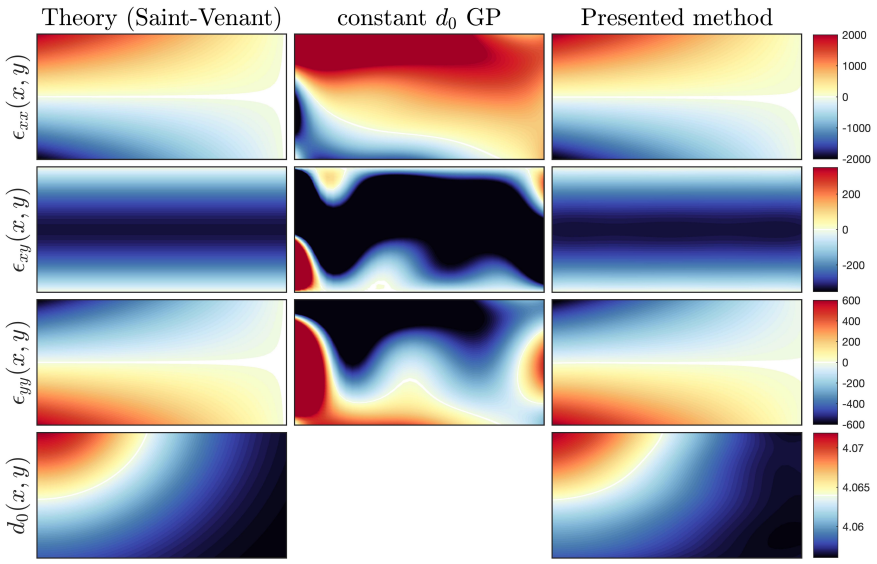


Figure 3: Simulation results for the cantilever beam strain field. The estimated strain field using the presented method is shown as well as the results of assuming a constant d_0 and applying standard GP regression. In the case of the presented method, the estimated d_0 field is also shown. Strain values are given in μStrain.

4.2 In-situ Loaded C-shape Sample

The method is now demonstrated on a more complex strain field given by FEA of a mild steel C-shape sample with geometry defined in Figure 4. The sample was subjected to a 7 kN compressive load distributed over 5° arcs and plane stress was assumed for the analysis. The resulting FEA strain field is shown in Figure 5. This sample and loading conditions correspond to the experimental setup used by Hendriks et al. (2017).

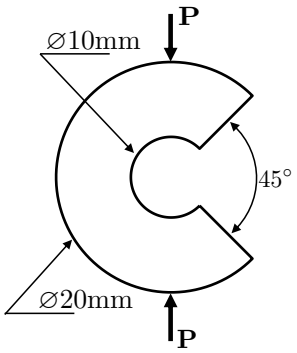


Figure 4: Geometry of the C-shape sample and in-situ loading **P**. The sample has an outer diameter of 20 mm and an inner diameter of 10 mm with a 45° segment removed. The sample was defined to have $E = 200$ GPa and $\nu = 0.28$.

Measurements of the form (3) were simulated through the this strain and a synthetic, smoothly changing d_0 field is again defined by Equation (25) with parameters given by $\{c_0, c_1, c_2, c_3, c_4, c_5\} = \{0.01, 5 \times 10^{-3}, 7.5 \times 10^{-3}, 7 \times 10^{-3}, 6 \times 10^{-3}, 4.056\}$. A total of 60 strain images were simulated with angles evenly spaced between 0° and 180°, and 180 measurements per image. The simulated measurements were corrupted with zero-mean noise of standard deviation $\sigma_n = c_5 \times 10^{-4}$ which is equivalent to 1×10^{-4} standard deviation in strain representing the typical experimental noise. A total of 131 zero-traction measurements were added around the boundary of the C-shape excluding the regions within 10° of the loading points. Reconstruction from the LRT and traction measurements was performed using both the presented method and the linear GP

regression method, and the results are shown in Figure 5.

The presented method achieves a mean relative error of 0.023 and it can be seen that the reconstruction has achieved the correct shape. Whereas assuming a constant d_0 value gives a mean relative error of 0.137 and the resulting strain fields show incorrect concentrated peaks in the strain field and areas of tension and compression that are reversed. Despite this improvement there is still some observable difference. In particular, the presented method has a concentrated tensile region on the top left boundary of the C, and does not capture the very concentrated peaks in magnitude on the inside of the C. These peak strains on the boundary are the hardest for the algorithm to reconstruct as they are poorly sampled by the LRT; i.e. they make up only a very small part of each line integral. Additionally, some of this remaining error is due to systematic error in the simulation of the measurements. Which are generated by numerically performing a line integral with each function evaluation being given by an interpolation of the FEA results.

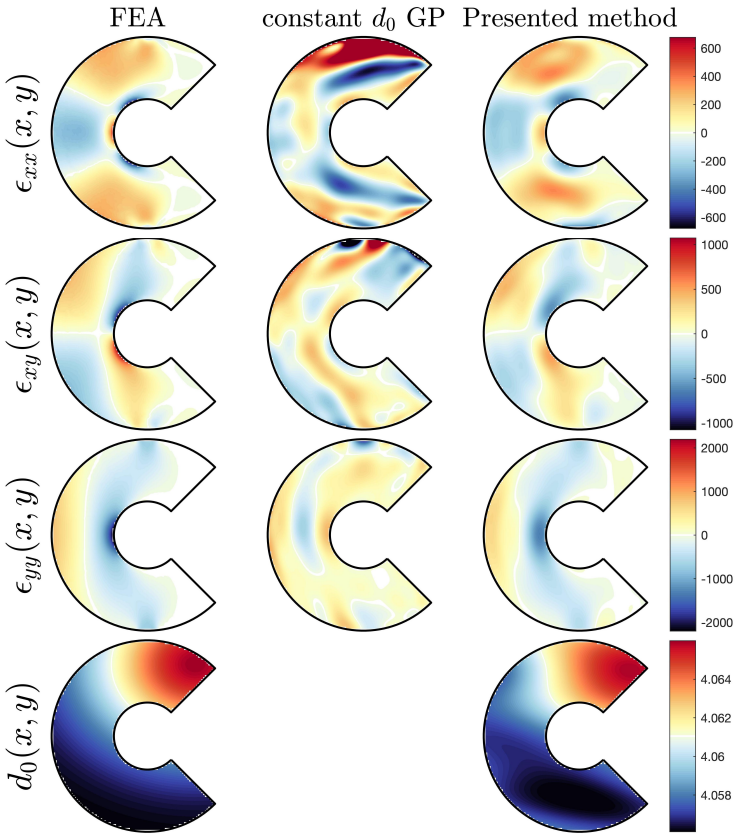


Figure 5: Simulation results for the FEA C-shape sample strain field. Strain values are given as μStrain. The estimated strain field using the presented method is shown as well as the results of assuming a constant d_0 and applying standard GP regression. In the case of the presented method, the estimated d_0 field is also shown.

5 Additional Remarks

5.1 Sensitivity to the Traction Measurement Variance

Boundary conditions given by unloaded surfaces are a natural inclusion as they are an artefact of the physical world. This information is included in the form of artificial measurements of zero traction, however it was found that a small variance needed to be placed on these measurements and the rate of convergence was

impacted by the size of this variance. Conceptually, this variance is analogous to a constraint tolerance for optimisation procedures. Too large a variance (or not enough traction measurements) and the algorithm may fail to converge to the correct strain field. This indicates that the traction measurements are ensuring that the problem is observable, which is supported by the findings of Hendriks et al. (2018b) where the inclusion of traction measurements allowed a constant d_0 value to be found as a hyperparameter. Conversely, too small a variance and the algorithm is unable to take optimisation steps of significant size, resulting in a large number of iterations to converge. Methods for optimally choosing this variance is an avenue for future research.

Despite this, it was found that the algorithm worked well over a reasonable range of traction variances. Typically the standard deviation of the traction measurements could be set two orders of magnitude smaller than the measurement standard deviation or in the range of 1×10^{-5} to 1×10^{-7}.

5.2 Hyperparameter Optimisation

The hyperparameters $\theta = \{l_x, l_y, \sigma_f\}$ can be found by performing an optimisation using $\mathcal{F}$ as the objective function. However, the gradients of $\mathcal{F}$ with respect to the GP hyperparameters are not trivial and so Steinberg and Bonilla (2014) suggests that gradient free optimisation approaches could be used. In this work, both Bayesian optimisation (Mockus, 2012) and the Nelda-Mead method (Nelder and Mead, 1965) were found to work; with the Nelda-Mead method requiring less computation time.

5.3 Computational cost

The majority of the computational burden comes from building the building the forward model of the LRT measurements. In particular, all the combinations of the basis function of the strain-free lattice spacing and the strain field need to be computed for each measurement. The resulting matrix has $nm_{d_0}m_{\varphi}$ elements. However, as this matrix only needs to be computed once, it is still feasible to solve even with a large number of basis functions.

6 Conclusion

This paper considers an extension of the strain tomography problem where the strain-free lattice parameter is a known constant, to the more general case where it is unknown and varies throughout the sample. A method for the joint reconstruction of a strain field and a varying strain-free lattice parameter from a set of neutron transmission strain images has been presented. This method extends the Gaussian process based approach previously used for strain tomography to the subsequently non-linear problem, and ensures that the estimated strain fields satisfy equilibrium and can include knowledge of boundary conditions. This was achieved by reformulating the problem in terms of basis functions and unknown coefficients. Variational inference was then employed to find estimates of the coefficients.

The method was tested on a set of simulated data, and importantly, these results demonstrate that it is possible to perform this joint reconstruction. Further, the results obtained by ignoring variations in d_0 and applying the linear GP regression method are provided and show that this assumption, if incorrect, severely degrades the accuracy of reconstruction.

Future work will involve planning an experiment to acquire a data set on which to further evaluate the methods performance.

A Basis Functions

The basis functions for the strain field were defined in (13) as

$$\phi_{\epsilon,j} = \begin{bmatrix} \frac{\partial^2}{\partial y^2} - \nu\frac{\partial^2}{\partial x^2} \\ -(1+\nu)\frac{\partial^2}{\partial x \partial y} \\ \frac{\partial^2}{\partial x^2} - \nu\frac{\partial^2}{\partial y^2} \end{bmatrix} \phi_{\varphi,j}. \tag{26}$$

As such, the components of $\phi_{\epsilon,j}$ can be built from

$$\begin{aligned} \frac{\partial^2}{\partial x^2}\phi_{\varphi,j} &= \frac{-\lambda_{\varphi x,j}^2}{\sqrt{L_{\varphi x} L_{\varphi y}}} \sin(\lambda_{\varphi x,j}(x + L_{\varphi x})) \sin(\lambda_{\varphi y,j}(y + L_{\varphi y})), \\ \frac{\partial^2}{\partial y^2}\phi_{\varphi,j} &= \frac{-\lambda_{\varphi y,j}^2}{\sqrt{L_{\varphi x} L_{\varphi y}}} \sin(\lambda_{\varphi x,j}(x + L_{\varphi x})) \sin(\lambda_{\varphi y,j}(y + L_{\varphi y})), \\ \frac{\partial^2}{\partial x \partial y}\phi_{\varphi,j} &= \frac{\lambda_{\varphi x,j}\lambda_{\varphi y,j}}{\sqrt{L_{\varphi x} L_{\varphi y}}} \cos(\lambda_{\varphi x,j}(x + L_{\varphi x})) \cos(\lambda_{\varphi y,j}(y + L_{\varphi y})). \end{aligned} \tag{27}$$

A predicted LRT measurement was defined by (14) as

$$y_* = \frac{1}{L}\int_0^L \bar{\mathbf{n}} \left(\sum_j \sum_k \phi_{\epsilon,j}(\mathbf{p} + \hat{\mathbf{n}}s) w_{\varphi,j} \phi_{d_0,k}(\mathbf{p} + \hat{n}s) w_{d_0,k} \right) + \left(\sum_k \phi_{d_0,k}(\mathbf{p} + \hat{n}s) w_{d_0,k} \right) \mathrm{d}s \tag{28}$$

where for clarity we restrict ourselves to a single measurement. Therefore, we need the components

$$\begin{aligned} &\int_0^L \phi_{d_0,k}(\mathbf{p} + \hat{\mathbf{n}}s)\, \mathrm{d}s, \\ &\int_0^L \phi_{d_0,k}(\mathbf{p} + \hat{\mathbf{n}}s) \left(\frac{\partial^2}{\partial x^2}\phi_{\varphi,j}(\mathbf{p} + \hat{\mathbf{n}}s) \right) \mathrm{d}s, \\ &\int_0^L \phi_{d_0,k}(\mathbf{p} + \hat{\mathbf{n}}s) \left(\frac{\partial^2}{\partial y^2}\phi_{\varphi,j}(\mathbf{p} + \hat{\mathbf{n}}s) \right) \mathrm{d}s, \\ &\int_0^L \phi_{d_0,k}(\mathbf{p} + \hat{\mathbf{n}}s) \left(\frac{\partial^2}{\partial x \partial x}\phi_{\varphi,j}(\mathbf{p} + \hat{\mathbf{n}}s) \right) \mathrm{d}s, \end{aligned} \tag{29}$$

To make the expressions briefer, we introduce the notation

$$\begin{aligned} \alpha_{\varphi x} &= \lambda_{\varphi x,j}(x_0 + \hat{n}_1 s + L_{\varphi x}), \quad \alpha_{\varphi y} = \lambda_{\varphi y,j}(y_0 + \hat{n}_2 s + L_{\varphi y}), \\ \alpha_{d_0 x} &= \lambda_{d_0 x,k}(x_0 + \hat{n}_1 s + L_{d_0 x}), \quad \alpha_{d_0 y} = \lambda_{d_0 y,k}(y_0 + \hat{n}_2 s + L_{d_0 y}). \end{aligned} \tag{30}$$

Giving

$$
\begin{aligned}
\zeta_k =& \int_0^L \phi_{d_0,k}(\mathbf{p}+\hat{\mathbf{n}}s)\,\mathrm{d}s \\
=& \frac{1}{\sqrt{L_{d_0x}L_{d_0y}}}\left(\frac{\sin(\alpha_{d_0x}-\alpha_{d_0y})}{2(\hat{n}_1\lambda_{d_0x,k}-\hat{n}_2\lambda_{d_0y,k})}-\frac{\sin(\alpha_{d_0x}+\alpha_{d_0y})}{2(\hat{n}_1\lambda_{d_0x,k}+\hat{n}_2\lambda_{d_0y,k})}\right)\Bigg|_{s=0}^{s=L}, \\
\psi_{1,kj} =& \int_0^L \phi_{d_0,k}(\mathbf{p}+\hat{\mathbf{n}}s)\left(\frac{\partial^2}{\partial x^2}\phi_{\varphi,j}(\mathbf{p}+\hat{\mathbf{n}}s)\right)\mathrm{d}s \\
=& \frac{-\lambda_{\varphi x,j}^2}{\sqrt{L_{\varphi x}L_{\varphi y}L_{d_0x}L_{d_0y}}}\left(-\Gamma_1-\Gamma_2+\Gamma_3+\Gamma_4-\Gamma_5+\Gamma_6-\Gamma_7+\Gamma_8\right)\Bigg|_{s=0}^{s=L}, \\
\psi_{2,kj} =& \int_0^L \phi_{d_0,k}(\mathbf{p}+\hat{\mathbf{n}}s)\left(\frac{\partial^2}{\partial y^2}\phi_{\varphi,j}(\mathbf{p}+\hat{\mathbf{n}}s)\right)\mathrm{d}s \\
=& \frac{-\lambda_{\varphi y,j}^2}{\sqrt{L_{\varphi x}L_{\varphi y}L_{d_0x}L_{d_0y}}}\left(-\Gamma_1-\Gamma_2+\Gamma_3+\Gamma_4-\Gamma_5+\Gamma_6-\Gamma_7+\Gamma_8\right)\Bigg|_{s=0}^{s=L}, \\
\psi_{3,kj} =& \int_0^L \phi_{d_0,k}(\mathbf{p}+\hat{\mathbf{n}}s)\left(\frac{\partial^2}{\partial x\partial y}\phi_{\varphi,j}(\mathbf{p}+\hat{\mathbf{n}}s)\right)\mathrm{d}s \\
=& \frac{\lambda_{\varphi x,j}\lambda_{\varphi x,j}}{\sqrt{L_{\varphi x}L_{\varphi y}L_{d_0x}L_{d_0y}}}\left(-\Gamma_1+\Gamma_2-\Gamma_3+\Gamma_4-\Gamma_5+\Gamma_6+\Gamma_7-\Gamma_8\right)\Bigg|_{s=0}^{s=L},
\end{aligned}
\tag{31a}
$$

where

$$
\begin{aligned}
\Gamma_1 &= \frac{\sin(\alpha_{d_0x}-\alpha_{\varphi x}+\alpha_{d_0y}+\alpha_{\varphi y})}{8(\hat{n}_1\lambda_{d_0x,k}-\hat{n}_1\lambda_{\varphi x,j}+\hat{n}_2\lambda_{d_0y,k}+\hat{n}_2\lambda_{\varphi y,j})}, \\
\Gamma_2 &= \frac{\sin(\alpha_{d_0x}-\alpha_{\varphi x}-\alpha_{d_0y}-\alpha_{\varphi y})}{8(\hat{n}_1\lambda_{d_0x,k}-\hat{n}_1\lambda_{\varphi x,j}-\hat{n}_2\lambda_{d_0y,k}-\hat{n}_2\lambda_{\varphi y,j})}, \\
\Gamma_3 &= \frac{\sin(\alpha_{d_0x}-\alpha_{\varphi x}+\alpha_{d_0y}-\alpha_{\varphi y})}{8(\hat{n}_1\lambda_{d_0x,k}-\hat{n}_1\lambda_{\varphi x,j}+\hat{n}_2\lambda_{d_0y,k}-\hat{n}_2\lambda_{\varphi y,j})}, \\
\Gamma_4 &= \frac{\sin(\alpha_{d_0x}+\alpha_{\varphi x}-\alpha_{d_0y}-\alpha_{\varphi y})}{8(\hat{n}_1\lambda_{d_0x,k}+\hat{n}_1\lambda_{\varphi x,j}-\hat{n}_2\lambda_{d_0y,k}-\hat{n}_2\lambda_{\varphi y,j})}, \\
\Gamma_5 &= \frac{\sin(\alpha_{d_0x}+\alpha_{\varphi x}+\alpha_{d_0y}-\alpha_{\varphi y})}{8(\hat{n}_1\lambda_{d_0x,k}+\hat{n}_1\lambda_{\varphi x,j}+\hat{n}_2\lambda_{d_0y,k}-\hat{n}_2\lambda_{\varphi y,j})}, \\
\Gamma_6 &= \frac{\sin(\alpha_{d_0x}-\alpha_{\varphi x}-\alpha_{d_0y}+\alpha_{\varphi y})}{8(\hat{n}_1\lambda_{d_0x,k}-\hat{n}_1\lambda_{\varphi x,j}-\hat{n}_2\lambda_{d_0y,k}+\hat{n}_2\lambda_{\varphi y,j})}, \\
\Gamma_7 &= \frac{\sin(\alpha_{d_0x}+\alpha_{\varphi x}-\alpha_{d_0y}+\alpha_{\varphi y})}{8(\hat{n}_1\lambda_{d_0x,k}+\hat{n}_1\lambda_{\varphi x,j}-\hat{n}_2\lambda_{d_0y,k}+\hat{n}_2\lambda_{\varphi y,j})}, \\
\Gamma_8 &= \frac{\sin(\alpha_{d_0x}+\alpha_{\varphi x}+\alpha_{d_0y}+\alpha_{\varphi y})}{8(\hat{n}_1\lambda_{d_0x,k}+\hat{n}_1\lambda_{\varphi x,j}+\hat{n}_2\lambda_{d_0y,k}+\hat{n}_2\lambda_{\varphi y,j})}.
\end{aligned}
\tag{31b}
$$

Returning to the measurement model in (14), we can now write

$$
y_* = \frac{1}{L}\left(\sum_k\sum_j \bar{\mathbf{n}}w_{d_0,k}w_{\varphi j}\begin{bmatrix}\psi_{2,kj}-\nu\psi_{1,kj}\\ -(1+\nu)\psi_{3,kj}\\ \psi_{1,kj}-\nu\psi_{2,kj}\end{bmatrix}_{s=0}^{s=L}+\sum_k w_{d_0,k}\zeta_k\Big|_{s=0}^{s=L}\right). \tag{31c}
$$

B Measurement Model Derivatives

Here we give the derivates of the measurement model $g(\cdot)$ about the current $\hat{\mathbf{w}}$. The measurement model is a concatenation of equations (14) and (15), and so we require the derivatives of the predicted LRT measurement, $\hat{y}$, and the predicted traction $\hat{y}_t$. For clarity we restrict the following to a single $\hat{y}$ and $\hat{y}_t$. The first derivatives are given by

$$\begin{aligned}
\frac{\partial \hat{y}}{\partial w_{d_0,k}} &= \frac{1}{L}\left(\sum_j \bar{\mathbf{n}} w_{\varphi *,j} \begin{bmatrix} \psi_{2,kj} - \nu\psi_{1,kj} \\ -(1+\nu)\psi_{3,kj} \\ \psi_{1,kj} - \nu\psi_{2,kj} \end{bmatrix}_{s=0}^{s=L} + \zeta_k\Big|_{s=0}^{s=L}\right), \\
\frac{\partial \hat{y}}{\partial w_{\varphi,k}} &= \frac{1}{L}\left(\sum_k \bar{\mathbf{n}} w_{d_0 *,k} \begin{bmatrix} \psi_{2,kj} - \nu\psi_{1,kj} \\ -(1+\nu)\psi_{3,kj} \\ \psi_{1,kj} - \nu\psi_{2,kj} \end{bmatrix}_{s=0}^{s=L}\right), \\
\frac{\partial \hat{y}_t}{\partial \mathbf{w}_{d_0}} &= 0, \\
\frac{\partial \hat{y}_t}{\partial \mathbf{w}_{\varphi}} &= \mathbf{T}\boldsymbol{\phi}_{\varphi}(\mathbf{x}).
\end{aligned} \tag{32}$$

The second derivates are

$$\begin{aligned}
\frac{\partial^2 \hat{\mathbf{y}}_t}{\partial \mathbf{w}^2} &= 0, \\
\frac{\partial^2 \hat{y}}{\partial \mathbf{w}^2} &= \begin{bmatrix} 0 & \frac{\partial^2 \hat{y}}{\partial \mathbf{w}_{d_0} \partial \mathbf{w}_{\varphi}} \\ \left(\frac{\partial^2 \hat{y}}{\partial \mathbf{w}_{d_0} \partial \mathbf{w}_{\varphi}}\right)^{\mathsf{T}} & 0 \end{bmatrix},
\end{aligned} \tag{33}$$

where

$$\left[\frac{\partial^2 \hat{y}}{\partial \mathbf{w}_{d_0} \partial \mathbf{w}_{\varphi}}\right]_{kj} = \bar{\mathbf{n}} \begin{bmatrix} \psi_{2,kj} - \nu\psi_{1,kj} \\ -(1+\nu)\psi_{3,kj} \\ \psi_{1,kj} - \nu\psi_{2,kj} \end{bmatrix}_{s=0}^{s=L}. \tag{34}$$

Explicit formulation of the second derivatives allows the cost functions curvature to be taken into account in the optimisation procedure, greatly improving the rate of convergence.

References

B Abbey, SY Zhang, W Vorster, and AM Korsunsky. Feasibility study of neutron strain tomography. *Procedia Engineering*, 1(1):185–188, 2009.

B Abbey, SY Zhang, W Vorster, and AM Korsunsky. Reconstruction of axisymmetric strain distributions via neutron strain tomography. *Nuclear Instruments and Methods in Physics Research Section B: Beam Interactions with Materials and Atoms*, 270:28–35, 2012.

FP Beer, ER Johnston Jr, JT Dewolf, and DF Mazurek. Mechanics of materials, sixth edit edition, 2010.

CM Bishop et al. *Neural networks for pattern recognition*. Oxford university press, 1995.

D Blei, A Kucukelbir, and J McAuliffe. Variational inference: A review for statisticians. *Journal of the American Statistical Association*, 112(518):859–877, 2017.

WB Choi, L Li, V Luzin, R Neiser, T Gnäupel-Herold, HJ Prask, S Sampath, and A Gouldstone. Integrated characterization of cold sprayed aluminum coatings. *Acta Materialia*, 55(3):857–866, 2007.

AWT Gregg, JN Hendriks, CM Wensrich, and MH Meylan. Tomographic reconstruction of residual strain in axisymmetric systems from bragg-edge neutron imaging. *Mechanics Research Communications*, 85:96–103, 2017.

AWT Gregg, JN Hendriks, CM Wensrich, Adrian Wills, AS Tremsin, Vladimir Luzin, Takenao Shinohara, Oliver Kirstein, MH Meylan, and EH Kisi. Tomographic reconstruction of two-dimensional residual strain fields from bragg-edge neutron imaging. *Physical Review Applied*, 10(6):064034, 2018.

J Hendriks. Joint tomography of strain and the strain-free lattice spacing from neutron transmission strain images. `https://github.com/jnh277/Joint_strain_d0_tomography.git`, 2019. URL `https://github.com/jnh277/Joint_strain_d0_tomography.git`.

JN Hendriks, AWT Gregg, CM Wensrich, AS Tremsin, T Shinohara, M Meylan, EH Kisi, V Luzin, and O Kirsten. Bragg-edge elastic strain tomography for in situ systems from energy-resolved neutron transmission imaging. *Physical Review Materials*, 1(5):053802, 2017.

JN Hendriks, AWT Gregg, CM Wensrich, and A Wills. Implementation of traction constraints in bragg-edge neutron transmission strain tomography. *arXiv preprint arXiv:1805.09760*, 2018a.

JN Hendriks, CM Wensrich, A Wills, V Luzin, and AW T Gregg. Robust inference of two-dimensional strain fields from diffraction-based. *arXiv preprint arXiv:1808.06282*, 2018b.

P Hennig and M Kiefel. Quasi-newton method: A new direction. *Journal of Machine Learning Research*, 14 (Mar):843–865, 2013.

C Jidling, N Wahlström, A Wills, and TB Schön. Linearly constrained Gaussian processes. In *Advances in Neural Information Processing Systems (NIPS)*, Long Beach, CA, USA, December 2017.

C Jidling, J Hendriks, N Wahlström, A Gregg, TB Schön, C Wensrich, and A Wills. Probabilistic modelling and reconstruction of strain. *Nuclear Instruments and Methods in Physics Research Section B: Beam Interactions with Materials and Atoms*, 436:141–155, 2018.

MI Jordan, Z Ghahramani, TS Jaakkola, and LK Saul. An introduction to variational methods for graphical models. *Machine learning*, 37(2):183–233, 1999.

HJ Kirkwood, SY Zhang, AS Tremsin, AM Korsunsky, N Baimpas, and B Abbey. Neutron strain tomography using the radon transform. *Materials Today: Proceedings*, 2:S414–S423, 2015.

WRB Lionheart and PJ Withers. Diffraction tomography of strain. *Inverse Problems*, 31(4):045005, 2015.

V Luzin, K Spencer, and M-X Zhang. Residual stress and thermo-mechanical properties of cold spray metal coatings. *Acta Materialia*, 59(3):1259–1270, 2011.

J Mockus. *Bayesian approach to global optimization: theory and applications*, volume 37. Springer Science & Business Media, 2012.

I Murray and RP Adams. Slice sampling covariance hyperparameters of latent gaussian models. In *Advances in neural information processing systems*, pages 1732–1740, 2010.

JA Nelder and R Mead. A simplex method for function minimization. *The computer journal*, 7(4):308–313, 1965.

A Papoulis and S Pillai. *Probability, random variables, and stochastic processes*. Tata McGraw-Hill Education, 2002.

A Paradowska, JWH Price, R Ibrahim, and T Finlayson. A neutron diffraction study of residual stress due to welding. *Journal of materials processing technology*, 164:1099–1105, 2005.

CE Rasmussen and CKI Williams. *Gaussian processes for machine learning*, volume 1. MIT press Cambridge, 2006.

MH Sadd. *Elasticity: theory, applications, and numerics*. Academic Press, 2009.

JR Santisteban, L Edwards, ME Fitzpatrick, A Steuwer, PJ Withers, MR Daymond, MW Johnson, N Rhodes, and EM Schooneveld. Strain imaging by bragg edge neutron transmission. *Nuclear Instruments and Methods in Physics Research Section A: Accelerators, Spectrometers, Detectors and Associated Equipment*, 481(1):765–768, 2002a.

JR Santisteban, L Edwards, ME Fizpatrick, A Steuwer, and PJ Withers. Engineering applications of Bragg-edge neutron transmission. *Applied Physics A*, 74(1):s1433–s1436, 2002b.

A Solin and S Särkkä. Hilbert space methods for reduced-rank gaussian process regression. *arXiv preprint arXiv:1401.5508*, 2014.

DM Steinberg and EV Bonilla. Extended and unscented gaussian processes. In *Advances in Neural Information Processing Systems*, pages 1251–1259, 2014.

AS Tremsin, JB McPhate, W Kockelmann, JV Vallerga, OHW Siegmund, and WB Feller. High resolution Bragg edge transmission spectroscopy at pulsed neutron sources: Proof of principle experiments with a neutron counting MCP detector. *Nuclear Instruments and Methods in Physics Research Section A: Accelerators, Spectrometers, Detectors and Associated Equipment*, 633:S235–S238, 2011.

AS Tremsin, JB McPhate, A Steuwer, W Kockelmann, A M Paradowska, JF Kelleher, JV Vallerga, OHW Siegmund, and WB Feller. High-resolution strain mapping through time-of-flight neutron transmission diffraction with a microchannel plate neutron counting detector. *Strain*, 48(4):296–305, 2012.

N Wahlström. *Modeling of Magnetic Fields and Extended Objects for Localization Applications*. PhD thesis, Linköping University Electronic Press, 2015.